

Key factors for methane combustion over palladium-based catalysts revealed by enhanced and depressed catalytic performance

Jia Lin^a, Jiangli Huang^a, Xiaohua Chen^a, Yong Zheng^b, Yihong Xiao^b, Ying Zheng^{a,*}, Lilong Jiang^b

^a College of Chemistry and Materials Science, Fujian Provincial Key Laboratory of Advanced Materials Oriented Chemical Engineering, Fujian Normal University, Fuzhou 350007, Fujian, PR China

^b National Engineering Research Center of Chemical Fertilizer Catalyst, Fuzhou University, Fuzhou 350002, Fujian, PR China



ARTICLE INFO

Keywords:

Methane combustion
 $\text{Sn}_x\text{Zr}_{1-x}\text{O}_2$ solid solutions
 Palladium catalysts
 Oxygen vacancies
 Support effect

ABSTRACT

In this work, metal oxides with different phase structures (stannic oxide, zirconia and tin-zirconium binary oxide) were designed to construct palladium-based catalysts. The factors affecting methane combustion over catalysts were revealed by exploring the reasons for the enhancement and depression of catalytic performance under various reaction conditions. The formation of $\text{Sn}_x\text{Zr}_{1-x}\text{O}_2$ solid solutions not only generated abundant oxygen vacancies to improve the reducibility of PdO and the redox of $\text{Pd} \leftrightarrow \text{PdO}$, but also induced the formation of active PdO_x , conjointly leading to the excellent catalytic activity and hydrothermal stability. Under SO_2 -containing atmosphere, the thermodynamically favorable formation of stable $\text{Zr}(\text{SO}_4)_2$ caused the significant diminish of oxygen vacancies and active Pd step sites in catalysts. Consequently, the sulfur-resistance and regeneration performance of Zr-containing catalysts were inferior to those of Pd/SnO_2 . The above contrast manifested that both oxygen vacancies and active palladium species were responsible for the efficient and stable methane combustion.

1. Introduction

Rising energy demand is causing an increased utilization of fossil fuels, resulting in the perpetual release of greenhouse gas- CO_2 and other pollutants [1–3]. In addition to capturing the pollutants or converting them into high value-added products, the development and utilization of cleaner energy is also an important solution [4,5]. Natural gas is a fossil fuel superior to coal and oil because its main component, methane, produces more heat and releases less CO_2 than other hydrocarbon fuels [6,7]. However, the utilization of natural gas by conventional flame combustion requires a high reaction temperature (>1400 °C), and releases unburnt CH_4 and toxic NO_x , which has a negative impact on the environment [1]. Catalytic combustion is a promising clean technology that can improve combustion efficiency, lower activation energy and reduce undesired by-products [8,9]. The noble metal-palladium has aroused great research interest in various catalytic applications [10,11]. Palladium-based catalysts are highly active for methane combustion [12–14], but the palladium species are easily sintered, decomposed and poisoned by water vapor or sulfur dioxide under reaction conditions

[15–17]. It remains challenging to construct Pd -based catalysts that exhibit both high catalytic activity and stability for practical applications.

Tuning the composition and microstructure of catalysts is considered to be effective in improving catalytic performance [18–20]. For methane combustion over Pd -based catalysts, CH_4 is generally oxidized by lattice oxygen of PdO_x or activated oxygen species on the catalyst [21,22]. The replenishment of lattice oxygen and the activation of surface oxygen species are closely related to the oxygen vacancies on the catalyst and the oxygen mobility of the support [23,24]. Hence, metal oxides with high oxygen mobility, such as Co_3O_4 , CeO_2 , and SnO_2 , are attractive for preparing Pd -based catalysts [22,25,26]. According to the high standard oxide formation enthalpy ($\Delta_f\text{H}_{\text{M}-\text{O}}^\circ$) of SnO_2 , its metal-oxygen bond is relatively weak [13], so lattice oxygen can be easily activated to produce abundant surface oxygen species. Coupled with its excellent thermal stability, the as-prepared Pd/SnO_2 catalyst exhibited relatively high catalytic activity for methane combustion even in the presence of 5 vol% water vapor [26,27]. The incorporation of additional metal components in Pd/SnO_2 can further optimize the structure, surface properties and

* Corresponding author.

E-mail address: zhengying@fjnu.edu.cn (Y. Zheng).

catalytic performance of the catalyst. CeO₂ is known for its high oxygen donation capacity and strong interaction with noble metals [28,29], which can facilitate the oxidation of palladium and generate active Pd^{δ+} ($0 < \delta < 2$) species for methane combustion [30]. As reported in our previous work, the coexistence of SnO₂ and CeO₂ phases in an appropriate ratio improved the redox of PdO→Pd and provoked superior catalytic activity and stability over Pd/Sn-Ce catalysts [31]. Similar to CeO₂, ZrO₂ also favors the oxygen exchange between PdO and the support. ZrO₂ supports prepared by chemical precipitation typically consist of a mixture of monoclinic (thermodynamically stable) and tetragonal (metastable) phases at low temperatures (< 1100 °C) [24, 32]. The composition of above mixed phases can be tuned by regulating the calcination temperature of the support or the metal-support interaction, then the induced phase transformation of ZrO₂ would give rise to abundant oxygen vacancies and high oxygen mobility, contributing to the oxidation of methane [24]. Moreover, ZrO₂ is an important component of the widely applied Pd/CeO₂-ZrO₂ catalyst. Modifying the structure or solid solution phase of CeO₂-ZrO₂ composites could optimize the dispersion, chemical state and redox property of palladium species, giving rise to higher catalytic activity [33,34]. Nevertheless, the synthesis of active kappa-phase Ce_xZr_{1-x}O₄ generally requires high-temperature reduction, and the resulted sintering of solid solutions was adverse to the dispersion of palladium species [33]. Meanwhile, the commercial Pd/CeO₂-ZrO₂ three-way catalysts still suffer from the thermal aging and sulfur-induced deactivation under real application conditions [35]. Considering the high thermal stability and oxygen mobility of SnO₂, the rational incorporation of ZrO₂ into Pd/SnO₂ is expected to provoke efficient and stable performance for methane combustion. It has been uncovered that the Sn_xZr_{1-x}O₂ solid solution supported palladium catalysts outperformed Pd/SnO₂ or Pd/ZrO₂ towards methane combustion under dry and sulfur-free conditions, and the catalyst with a certain Sn/Zr ratio showed excellent catalytic activity due to the high oxygen mobility and moderate reducibility [36]. However, the relationship between the phase structure of SnO₂-ZrO₂ composite supports and the catalytic performance of Pd-based catalysts has not been elucidated. The effects of water vapor and sulfur species in the reaction atmosphere on the structure, oxygen mobility and catalytic performance of Pd/Sn-Zr catalysts need to be explored for rational design of catalysts.

Herein, SnO₂-ZrO₂ binary oxides with different phase structures were synthesized through a strategy combining co-precipitation and hydrothermal crystallization methods. For comparison, palladium-based catalysts were prepared with above binary or unary oxide supports. The catalytic activity and stability of catalysts for methane combustion under various conditions (in the absence and presence of water vapor/SO₂) were systematically investigated. The influence of the support composition on the phase structure, redox properties and active palladium species of the catalysts was explored. The key factors for the enhancement of catalytic performance under sulfur-free atmosphere were revealed, and the reason why the presence of SO₂ in feed gas led to catalyst deactivation was clarified. This study brings new insights into the structure-performance relationship of Pd-based catalysts for methane combustion, emphasizing the importance of support design.

2. Experimental

2.1. Preparation of supports

The SnO₂-ZrO₂ binary oxide supports were synthesized by the combination of co-precipitation and hydrothermal crystallization route. i) The required amount of SnCl₄·5 H₂O and ZrO(NO₃)₂·xH₂O precursors (10 mmol in total) were dissolved in 60 mL of deionized water under continuous stirring at room temperature. ii) Subsequently, n-butylamine (mass fraction= 98 %) was added dropwise to the above mixture with stirring until the pH reached ca. 9.5. iii) After stirring for 2 h, the mixture was hydrothermally treated at 120 °C for 3 h and cooled to room

temperature, then filtered and washed with deionized water. iv) The precipitate was dried at 80 °C for 12 h and then calcined in air at 500 °C and 1000 °C for 3 h sequentially. The obtained support was denoted as xSn(10-x)Zr, where x represented the molar content of Sn component in the catalyst determined by ICP-OES (x = 10, 8.9, 7.2, 4.7, 2.6, 0, assuming that the total content of Sn and Zr in the catalyst was 10 mmol) (Table S1).

2.2. Preparation of catalysts

Taking xSn(10-x)Zr as supports, palladium-based catalysts (theoretical loading content of Pd: 0.5 wt%, actual content: 0.39–0.45 wt%) (Table S1) were synthesized by impregnation method as mentioned before [31]. The catalyst precursor was dried at 80 °C and then calcined at 600 °C for 3 h. The synthesized catalyst was labeled as Pd/xSn(10-x)Zr.

2.3. Characterization

The physicochemical properties of supports and catalysts were characterized by X-ray powder diffraction (XRD), Raman spectroscopy, N₂ physisorption measurements, transmission electron microscopy (TEM), X-ray photoelectron spectroscopy (XPS), temperature-programmed desorption of O₂ (O₂-TPD), temperature-programmed oxidation of O₂ (O₂-TPO), temperature-programmed reduction of CH₄ (CH₄-TPR) and H₂ (H₂-TPR), in-situ diffuse reflectance infrared Fourier transform spectroscopy study of CO adsorption (CO-DRIFTS), and Fourier transform infrared spectroscopy (FTIR). The chemical composition of catalysts was determined by ICP-OES analysis. The electrical conductivity of catalysts was investigated via the two-electrode method. Experimental details were presented in Section S1 of the Supplementary material.

2.4. Evaluation of catalytic performance

The baseline catalytic activity of Pd/xSn(10-x)Zr for methane combustion (procedure “a” of Fig. S1) was explored at atmospheric pressure, using a conventional fixed-bed reactor containing a U-shaped quartz tube. The test was conducted under the following conditions. Catalyst dosage: 100 mg of catalyst (30–80 mesh) was diluted with 1000 mg of quartz sand; feed gas composition: 1 vol% CH₄ and 5 vol% O₂ were balanced in N₂; total weight hourly space velocity (WHSV): 50,000 mL·g⁻¹·h⁻¹. For comparison, the stability and hydrothermal stability of Pd/10Sn, Pd/10Zr and Pd/7.2Sn2.8Zr catalysts were further studied through on-stream tests in the absence and presence of 5 vol% or 8 vol% water vapors (procedure “b” and “c” of Fig. S1). The sulfur-resistance of Pd/10Sn, Pd/10Zr and Pd/7.2Sn2.8Zr catalysts in methane combustion was investigated in the presence of 5 ppm SO₂ (SO₂ concentrations in natural gas engine exhaust are typically below 5 ppm [37]) during the light-off and on-stream tests (procedure “d” and “e” of Fig. S1). Afterward, the sulfated catalysts were regenerated sequentially through the light-off tests from 250° to 600 °C (with a rate of 1.5 °C·min⁻¹) and on-stream tests at 420 °C for 10 h without SO₂ (procedure “f” and “g” of Fig. S1). More details were provided in section S2 and Fig. S1 of the Supplementary material.

3. Results and discussion

3.1. Catalytic performance of catalysts

3.1.1. Catalytic performance in the absence of SO₂

As shown in Fig. 1A, the baseline catalytic activity of catalysts was contingent on the composition of supports, and the activity of Sn-containing catalysts was higher than that of Pd/10Zr. Among the catalysts, Pd/7.2Sn2.8Zr exhibited excellent activity with a *T*₉₀ (temperature for 90 % methane conversion) of ca. 400 °C, much lower than Pd/10Zr

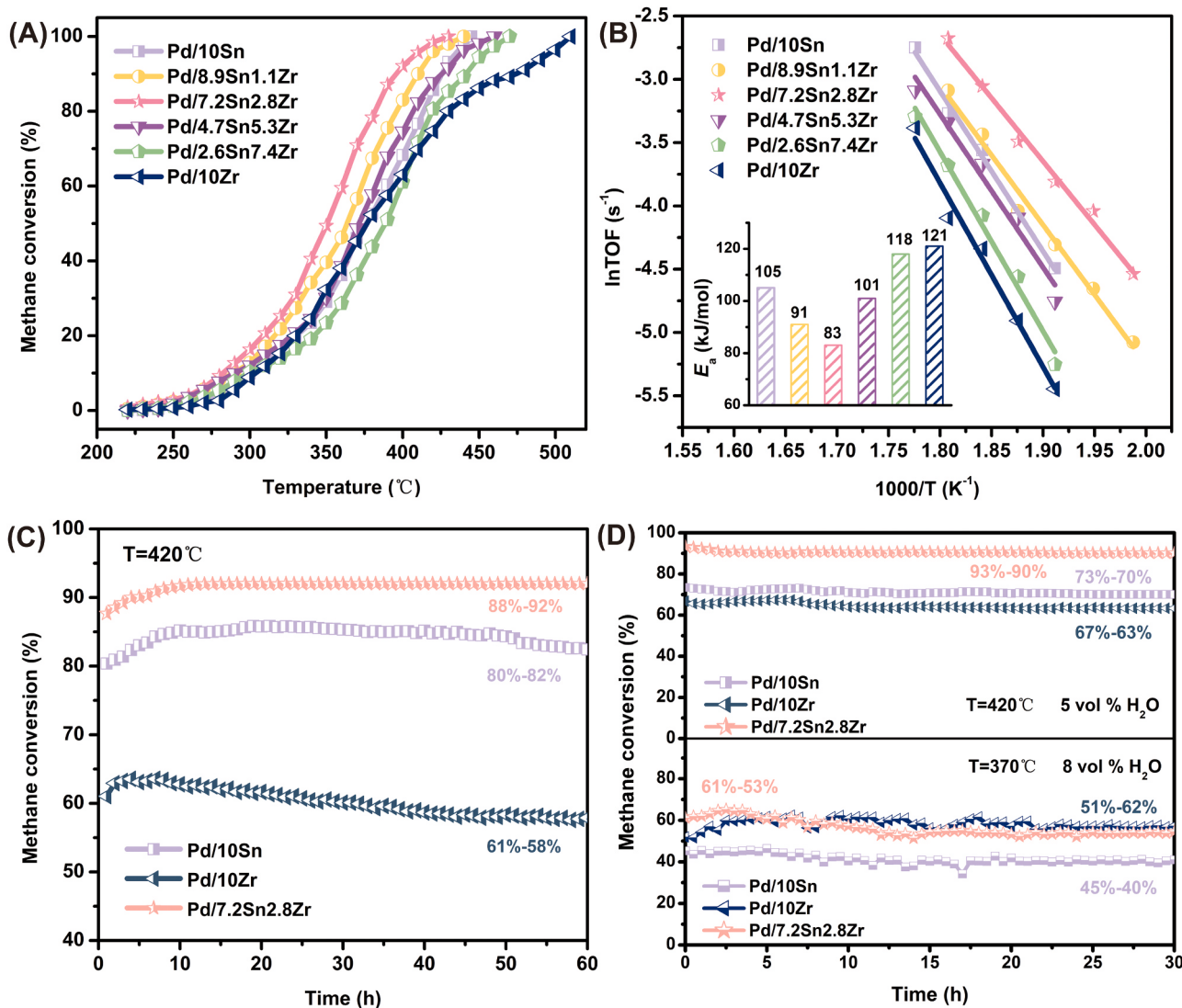


Fig. 1. Light-off curves (A), Arrhenius plots and E_a (inset, $X_{CH_4} < 10\%$) (B) of Pd/ x Sn(10- x)Zr catalysts in methane combustion, on-stream tests at 420 °C for 60 h under dry conditions (C) and at designated temperatures for 30 h under wet conditions (5 vol% H₂O at 420 °C and 8 vol% H₂O at 370 °C) (D) over Pd/10Sn, Pd/10Zr and Pd/7.2Sn2.8Zr catalysts.

(ca. 480 °C) and Pd/10Sn (ca. 430 °C) catalysts. The different catalytic activities of the catalysts were confirmed by parallel tests (Fig. S2). From Fig. 1B and Table S2, the relatively low E_a (activation energy), high r (reaction rate) and TOF (turnover frequency) values of Pd/7.2Sn2.8Zr demonstrated its superior catalytic activity. Given the relatively low Pd loading and high WHSV conditions, the catalytic activity of Pd/7.2Sn2.8Zr is comparable to the reported active Pd-based catalysts prepared with various supports (Table S3-1 and S3-2). Moreover, Pd/7.2Sn2.8Zr also showed high thermodynamic equilibrium conversion and CO₂ selectivity (Fig. S3), indicating that the rational construction of SnO₂-ZrO₂ binary oxide supports could provoke excellent catalytic activity and selectivity of Pd-based catalysts for methane combustion.

The catalytic performance of the active Pd/7.2Sn2.8Zr catalyst was further investigated through on-stream tests and compared with Pd/10Sn and Pd/10Zr. Fig. 1C showed that the catalytic activity and stability of Pd/10Zr were inferior to those of Pd/10Sn and Pd/7.2Sn2.8Zr at 420 °C under dry conditions. Despite the methane conversion of Pd/10Zr increased from 61 % to 65 % in the former 5 h, it decreased to 58 % at the end of the 60 h test. As for Pd/10Sn, the methane conversion also experienced a slight rise and fall during the test, but it could be kept above 80%, indicating the good catalytic stability, which was consistent

with the previous finding [26]. In the case of Pd/7.2Sn2.8Zr, methane conversion gradually increased from 88 % to 92 in the former 10 h, and was well-retained during the test. It has been uncovered that fluctuations in methane conversion during on-stream tests could be attributed to surface reconstruction of the working catalyst, and the catalytic activity was highly dependent on activation barriers over newly formed active sites [38]. Hence, it is inferred that the methane oxidation reaction induced the formation of highly active sites on Pd/7.2Sn2.8Zr.

The on-stream tests were further performed under wet conditions over fresh catalysts (Fig. 1D). With the introduction of 5 vol% H₂O at 420 °C, the methane conversion over Pd/10Sn fluctuated between 73 % and 70 %, which was lower than that under dry conditions. The loss of activity was also observed on Pd/10Sn at 370 °C in the presence of 8 vol % H₂O, which could be attributed to the blockage of active sites by the aggregation of hydroxyl groups on the catalyst surface [39]. This phenomenon was different from the previously reported Pd/SnO₂ catalysts with high water-resistance [27], which could be due to their differing microstructures. Surprisingly, the methane conversion of Pd/10Zr was maintained at 63–67% in the presence of 5 vol% H₂O at 420 °C, which was higher than that obtained under dry conditions. Moreover, the conversion rate on Pd/10Zr increased from 51 % to 62 % during the test

at 370 °C with 8 vol% H₂O. The enhanced catalytic activity could be related to the water-induced increase of grain boundaries, which promoted the activation of C-H bond [10], or to the facilitated oxidation of metallic Pd under wet conditions [40]. As for Pd/7.2Sn2.8Zr, it maintained a steady high conversion rate (93 %–90 %) at 420 °C with 5 vol % H₂O. Although the conversion rate on Pd/7.2Sn2.8Zr decreased more obviously at 370 °C with 8 vol% H₂O, it still maintained a relatively high activity during the reaction. Fig. S4 presented the T_{90} of fresh and hydrothermally aged catalysts. It was found that after removing water vapor, the T_{90} of the aged Pd/10Sn was higher than that of the corresponding fresh catalyst. By contrast, the catalytic activity of the aged Pd/7.2Sn2.8Zr and Pd/10Zr was recovered or even improved. The above results revealed that the Sn-containing catalyst exhibited higher catalytic activity for methane oxidation, while the Zr component could provoke better water-resistance of the catalyst. The Pd/7.2Sn2.8Zr catalyst with a moderate Sn/Zr molar ratio demonstrated excellent catalytic activity, stability and water resistance, which is among the state-of-the-art Pd-based catalysts (Table S3-1 and S3-2).

3.1.2. Sulfur resistance of catalysts towards methane combustion

Fig. 2A and B revealed the inhibitory effect of SO₂ on methane combustion over the catalysts. Compared with the baseline activity of

the catalysts (Fig. 1A), the introduction of SO₂ caused a slight decrease in the catalytic activity of Pd/10Sn, while the activity loss of Pd/7.2Sn2.8Zr and Pd/10Zr was more pronounced. Nevertheless, Pd/7.2Sn2.8Zr still afforded a relatively high methane conversion in the presence of SO₂. In view of the decreased reaction rate and increased E_a of sulfated catalysts (Fig. S5A and Table S4), it is deduced that the presence of SO₂ inhibited the activation and conversion of methane on catalysts.

Fig. 2C displayed the variation in methane conversion over catalysts during on-stream tests under SO₂-containing atmosphere. Significant deactivation was detected on Pd/7.2Sn2.8Zr, as the methane conversion dropped abruptly from 61 % to ca. 20 % in the first 1 h and gradually decreased to 12 % in the following 9 h. The Pd/10Zr catalyst was also severely deactivated by SO₂, which showed negligible activity (13–2 %) during the test. Pd/10Sn demonstrated better sulfur-resistance with a smaller decrease of methane conversion (48–22 %). Subsequently, the sulfated catalysts were tested for methane combustion in a sulfur-free atmosphere to investigate the regeneration performance. From the light-off curves during generation (Fig. 2A), methane conversion rate at 420 °C (Fig. 2B), E_a and reaction rate (Fig. S5B, Table S4) of catalysts, it was found that the catalytic activity of sulfated Pd/10Sn was largely restored via the oxidation reaction. The conversion rate during the

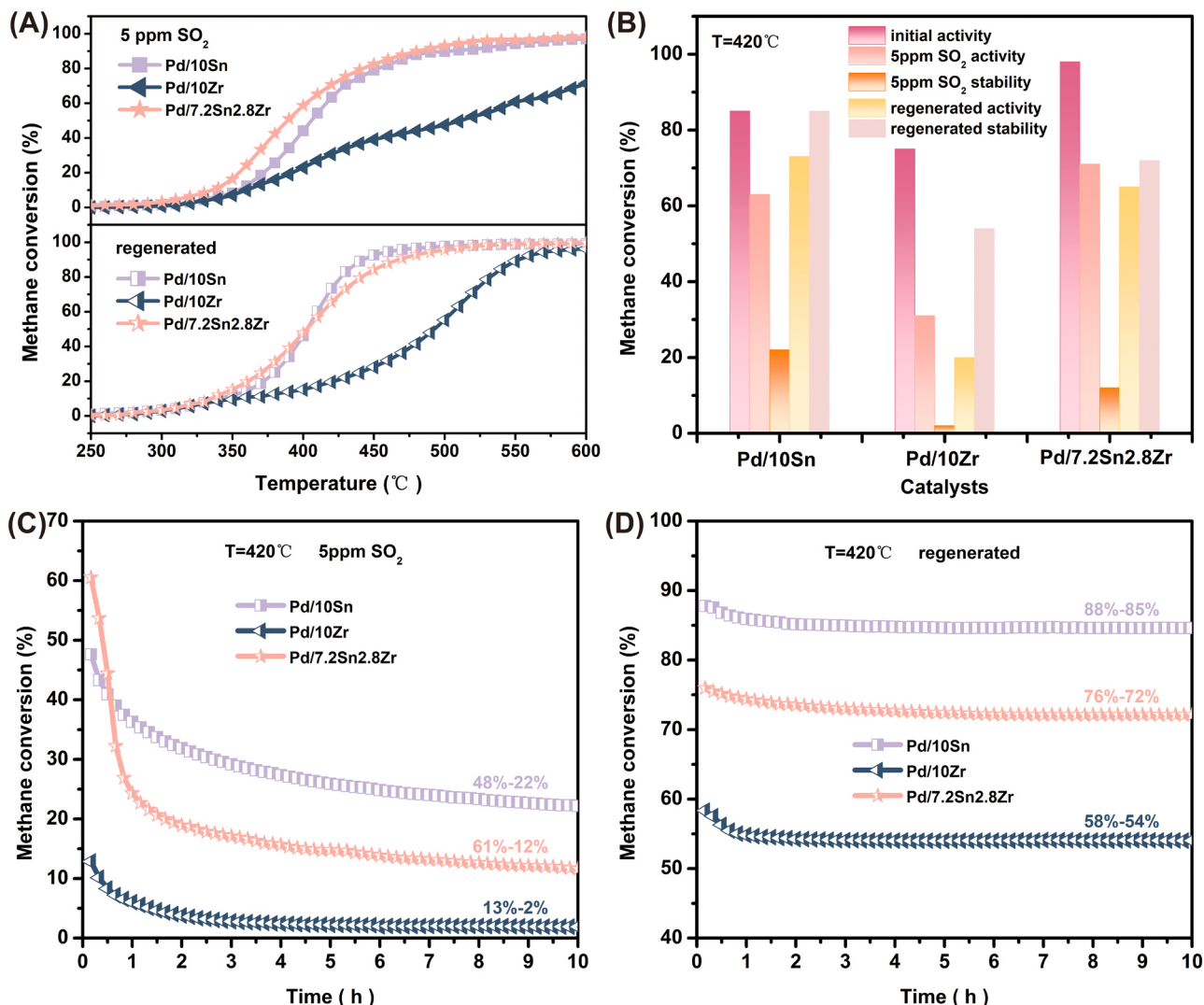


Fig. 2. Light-off curves for methane combustion over Pd/10Sn, Pd/10Zr and Pd/7.2Sn2.8Zr in the presence of 5 ppm SO₂ and after regeneration treatment (A), methane conversion of Pd/10Sn, Pd/10Zr and Pd/7.2Sn2.8Zr at 420 °C during different reactions (B), on-stream tests over Pd/10Sn, Pd/10Zr and Pd/7.2Sn2.8Zr at 420 °C in the presence of 5 ppm SO₂ (C) and after regeneration (D).

regeneration of Pd/10Zr was significantly lower than that in the baseline activity test, indicating that Pd/10Zr could not be effectively regenerated through the light-off test. The activity of Pd/7.2Sn2.8Zr partially recovered in the light-off test, but it was still inferior to the initial activity of the fresh catalyst. Afterward, catalysts were subjected to the on-stream tests in the absence of SO₂ (Fig. 2D), and they could retain steady conversion of methane without obvious loss of activity. Notably, the regenerated Zr-containing catalysts had a lower methane conversion rate than the regenerated Pd/10Sn that showed enhanced activity compared to the fresh one in the on-stream test. As mentioned above, Pd/7.2Sn2.8Zr presented excellent catalytic activity, stability and water resistance for methane combustion in the absence of SO₂, and Pd/10Zr demonstrated high water resistance. However, the above two catalysts were deactivated by the introduction of SO₂ in the feed gas, and could not be effectively regenerated through methane combustion under sulfur-free conditions. In contrast, Pd/10Sn showed an inferior water-resistance to Pd/7.2Sn2.8Zr and Pd/10Zr, but it exhibited an improved sulfur-resistance and regeneration performance. The structure and surface properties of the above catalysts were analyzed to clarify the reasons for the different catalytic performances.

3.2. Structural and surface properties of catalysts

3.2.1. Structure and morphology of fresh catalysts

In Fig. 3A, the characteristic peaks of tetragonal rutile SnO₂ (JCPDS

No. 41-1445) were identified for Sn containing supports. The diffraction peaks of *m*-ZrO₂ (JCPDS No. 37-1484) and *t*-ZrO₂ (JCPDS No. 50-1089) were observed over Zr-rich ($n_{\text{Zr}}/n_{\text{Sn}} \geq 1$) supports, while they were not detected over Sn-rich ($n_{\text{Zr}}/n_{\text{Sn}} < 1$) supports. With the increase of Zr content, the diffraction peak of SnO₂ (110) plane weakened and shifted to lower angles. It could be attributed to the substitution of Sn⁴⁺(0.71 Å) by Zr⁴⁺(0.79 Å) in the SnO₂ lattice, causing lattice expansion and increased lattice strain of SnO₂ (Table S5). Compared with the 10Zr support, the diffraction peaks associated with the ZrO₂ (-111) plane in the 2.6Sn7.4Zr and 4.7Sn5.3Zr supports slightly shifted to higher angles, which may be due to the incorporation of Sn⁴⁺ into the ZrO₂ lattice, inducing the lattice shrinkage of ZrO₂. The above variations in the lattice parameters of SnO₂ and ZrO₂ indicated the formation of Sn_xZr_{1-x}O₂ solid solutions [36]. It is inferred that the Zr component mainly entered the SnO₂ lattice to form a solid solution when the incorporation content was low ($n_{\text{Zr}}/n_{\text{Sn}} < 1$). At higher incorporation contents ($n_{\text{Zr}}/n_{\text{Sn}} \geq 1$), the ZrO₂ phase coexisted with the solid solution over catalysts. Furthermore, the grain sizes of SnO₂ and ZrO₂ in the binary oxides were smaller than those of the unary oxides (Table S5), suggesting that the interaction between the Sn and Zr components inhibited the grain growth to some extent [41].

From Fig. 3B, the XRD pattern of the catalyst was similar to that of the corresponding support. The characteristic peak of PdO or Pd was not observed over catalysts, which could be related to the low loading content or the high dispersion of palladium species on the catalyst

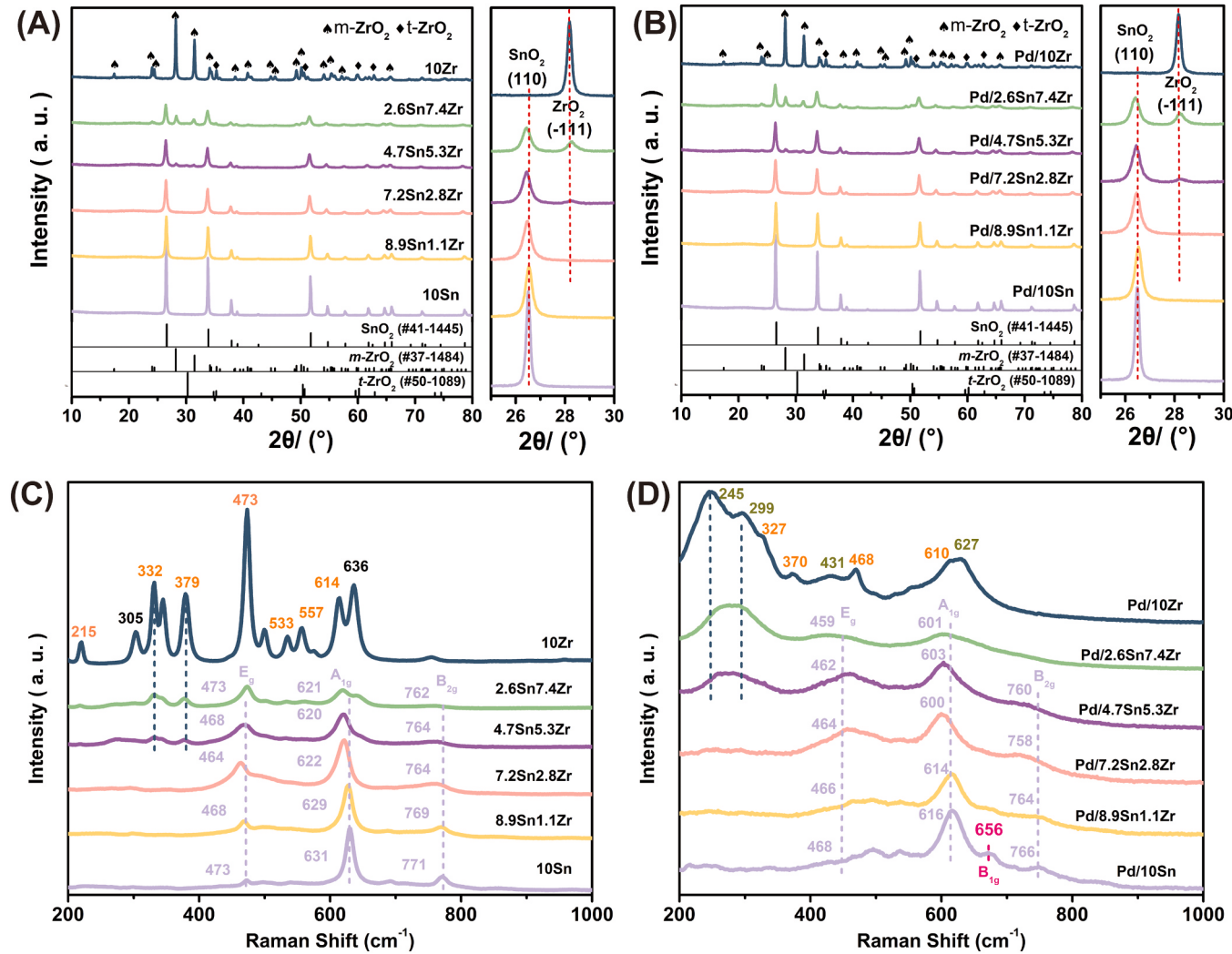


Fig. 3. Wide-angle XRD patterns and Raman spectra of xSn(10-x)Zr supports (A, C) and Pd/xSn(10-x)Zr catalysts (B, D).

surface [42]. It is found that the lattice parameters of SnO_2 or ZrO_2 increased slightly after loading palladium species (Table S6), which may be resulted from the incorporation of Pd^{2+} (0.86 Å) into the lattice of metal oxide supports, inducing the expansion of lattice [26].

From the Raman spectra of supports (Fig. 3C), bands assigned to $t\text{-}\text{ZrO}_2$ (305, 636 cm⁻¹) and $m\text{-}\text{ZrO}_2$ (215, 332, 379, 473, 533, 557, 614 cm⁻¹) were detected on the 10Zr support [43]. As to the 10Sn support, bands detected around 473, 631 and 771 cm⁻¹ were related to the E_g , A_1g and B_2g vibration modes of SnO_2 [44,45]. The characteristic bands ascribed to SnO_2 were observed in the binary oxide supports, which weakened and shifted to lower wavenumbers with the increase of Zr content. This phenomenon was attributed to the substitution of Sn^{4+} by Zr^{4+} with larger ionic radius, which may produce oxygen vacancies to generate structural distortion and weaken the Sn-O bond [45], further verifying the formation of $\text{Sn}_{x}\text{Zr}_{1-x}\text{O}_2$ solid solution. Moreover, bands associated with ZrO_2 were observed on supports with high Zr content ($n_{\text{Zr}}/n_{\text{Sn}} \geq 1$), indicating the formation of ZrO_2 , which was in accordance with the XRD analysis.

Compared with that of supports, the Raman bands of catalysts broadened and attenuated (Fig. 3D), manifesting the weakened M-O bond of oxides, which may be due to the interaction between the active palladium species and supports. The band at ca. 656 cm⁻¹ over Pd/10Sn corresponded to the B_1g mode of PdO [46], suggesting the existence of PdO on catalyst surface. In the Zr-containing catalysts, the bands of the PdO B_1g vibration mode were indistinguishable, but the broad peak shoulder at 600–700 cm⁻¹ could be related to the presence of PdO . For Pd/10Zr, the spectrum was quite different from that of the support. The bands detected at 245, 299, 431 and 627 cm⁻¹ belonged to the $c\text{-}\text{ZrO}_2$ phase [47], which were not reflected in the XRD pattern. Considering that Raman spectra are dominated by oxygen lattice vibrations and could provide surface information [48], while XRD patterns reveal the bulk phase structure [44], it is deduced that the additional calcination due to the loading of palladium species gave rise to $c\text{-}\text{ZrO}_2$ phase on the surface of Pd/10Zr. The textural properties of catalysts were investigated. From Table S7, the catalysts exhibited relatively low specific surface area (S_{BET}) (2.8–8.1 m² g⁻¹) and large pore size (22.9–47.9 nm), which could be ascribed to the high-temperature (1000 °C) calcination of the supports. It has been uncovered that the large S_{BET} and mesopores of catalysts would improve the dispersion of active sites and increase the contact area [18]. The S_{BET} of catalysts prepared with binary oxide supports was slightly higher than that of Pd/10Sn and Pd/10Zr, but the small difference may not have a significant impact on the catalytic performance.

The TEM images (Figs. S6A-C) showed that the nanoparticles in catalysts were of different sizes. Coupled with the EDS elemental analysis (Fig. S7), it is inferred that Pd/10Sn consisted of irregular SnO_2 nanoparticles (ca. 30–100 nm), and Pd/10Zr was composed of ZrO_2 nanoparticles with sizes of 50–100 nm, while Pd/7.2Sn2.8Zr was assembled from relatively small (ca. 20–30 nm) $\text{SnO}_2\text{-}\text{ZrO}_2$ nanoparticles. In Fig. S7, the uniform distribution of Sn and Zr elements over Pd/7.2Sn2.8Zr further verified the formation of homogeneous

$\text{Sn}_{x}\text{Zr}_{1-x}\text{O}_2$ solid solution. In addition, it could be observed that palladium species with different particle sizes (ca. 5–10 nm) were distributed on catalysts. The palladium particle sizes derived from the HAADF-STEM images were consistent with the results of the H_2 -chemisorption analysis listed in Table S2 (4.2–8.2 nm).

In the HRTEM image of Pd/10Sn (Fig. 4A), the interplanar spacing of 0.337 nm and 0.229 nm was ascribed to the SnO_2 (110) and (111) planes, respectively. For Pd/10Zr (Fig. 4B), the (−111) plane ($d=0.316$ nm) and (211) plane ($d=0.205$ nm) of $m\text{-}\text{ZrO}_2$, as well as (011) plane ($d=0.296$ nm) of $t\text{-}\text{ZrO}_2$ were observed. In the case of Pd/7.2Sn2.8Zr (Fig. 4C), the lattice spacing ascribed to SnO_2 (110) ($d=0.339$ nm) and (111) ($d=0.230$ nm) planes was slightly larger than the corresponding spacing in Pd/10Sn, indicating the expansion of SnO_2 lattice. Combined with the lattice distortion observed on Pd/7.2Sn2.8Zr, it could be deduced that Zr atoms entered the SnO_2 lattice, resulting in the formation of $\text{Sn}_{x}\text{Zr}_{1-x}\text{O}_2$ solid solutions, which was coincided with the XRD results. Furthermore, the lattice fringes attributed to PdO (101) plane were observed in the above catalysts, manifesting the presence of PdO phase. Interestingly, besides PdO particles, some flat nanoparticles (ca. 2 nm) appeared on the surface of Pd/7.2Sn2.8Zr. From the enlarged HRTEM images (Fig. S8), the lattice fringes of these nanoparticles were indistinguishable, indicating that they were in an amorphous state. It was found that amorphous PdO_x particles would exist on the surface of CeO_2 or $\text{CeO}_2\text{-}\text{SnO}_2$ supports due to the formation of Pd-containing solid solution [49,50]. Since Pd atoms may enter the SnO_2 lattice of Pd/7.2Sn2.8Zr, the detected amorphous nanoparticles can be assigned to the PdO_x species. As reported in the literature, the methane oxidation activity of catalysts was linearly correlated with the amount of surface PdO_x [51], it is deduced that the presence of abundant PdO_x on Pd/7.2Sn2.8Zr contributed to its superior catalytic activity.

3.2.2. The redox properties of fresh catalysts

The oxygen species on supports and catalysts were investigated by O_2 -TPD experiments. From Fig. S9A, the desorption of surface adsorbed oxygen species (O_2), active oxygen species (O^\cdot) and lattice oxygen species (O^{2-}) over supports were observed at 250–400 °C, 400–600 °C and 600–800 °C, respectively [52,53]. For 7.2Sn2.8Zr, a distinct desorption peak of O^\cdot was detected at a relatively low temperature, indicating the presence of abundant active oxygen species with high mobility [54]. As uncovered by the XRD analysis, the Zr component entered into the SnO_2 lattice over 4.7Sn5.3Zr and 7.2Sn2.8Zr, while ZrO_2 and $\text{Sn}_{x}\text{Zr}_{1-x}\text{O}_2$ solid solution coexisted in 4.7Sn5.3Zr and 2.6Sn7.4Zr. Hence, it is inferred that the formation of solid solution was conducive to the generation of oxygen vacancies and the activation of gaseous oxygen, while the presence of ZrO_2 may block the oxygen vacancies and was adverse to the formation of active oxygen species. In Fig. 5A, the peaks at 600–720 °C on catalysts were mainly ascribed to the desorption of lattice oxygen species (O^{2-}) from PdO [55]. The desorption peak on Pd/7.2Sn2.8Zr appeared at a lower temperature, which was associated with the generation of abundant oxygen vacancies. The oxygen vacancies would share the lattice oxygen of PdO_x , resulting in the weakened Pd-O bond

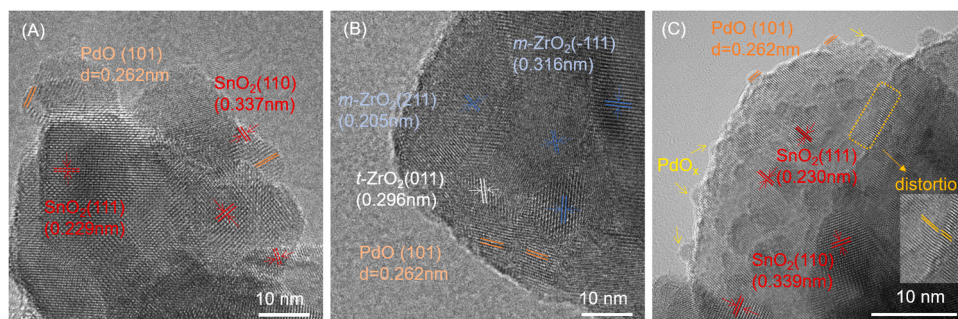


Fig. 4. HRTEM images of fresh Pd/10Sn (A), Pd/10Zr (B) and Pd/7.2Sn2.8Zr (C) catalysts.

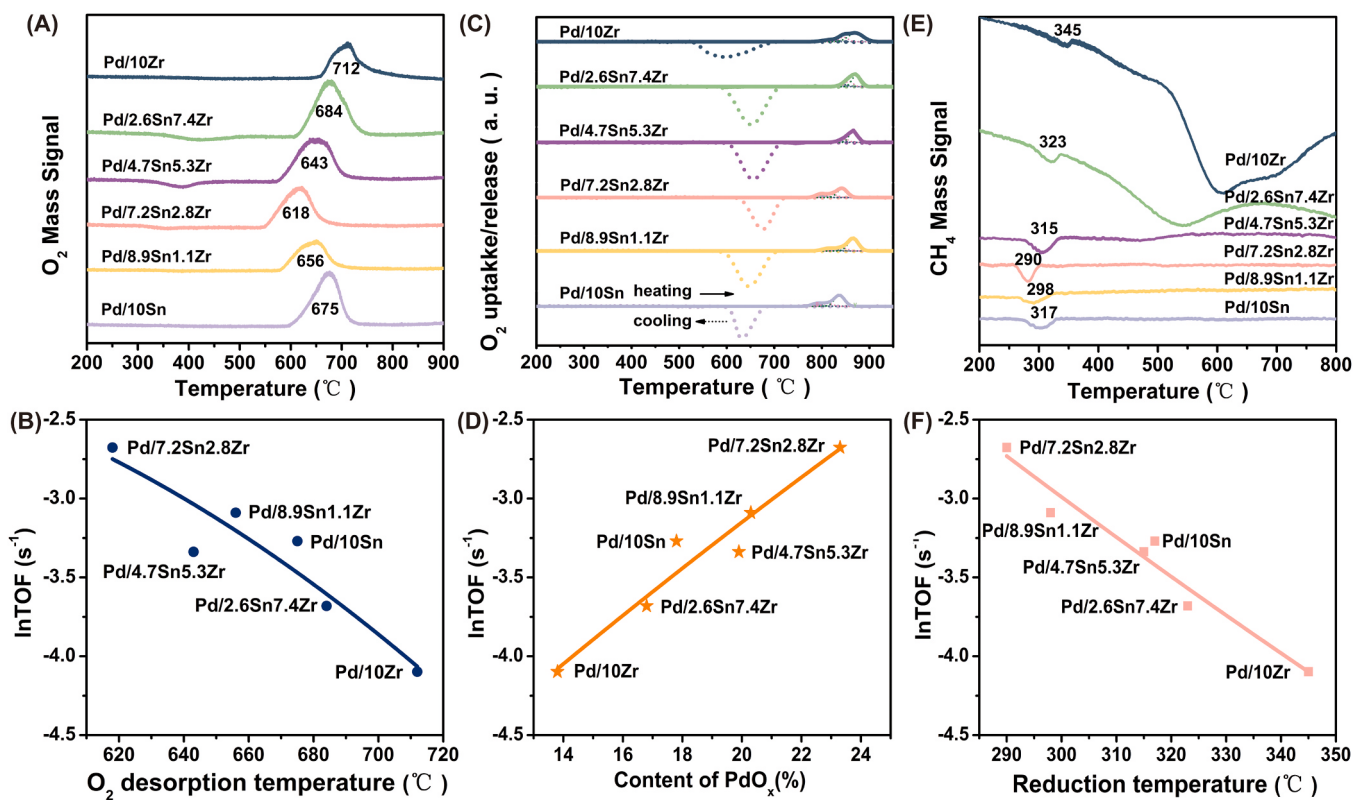


Fig. 5. O₂-TPD (A), O₂-TPO (C) and CH₄-TPR (E) profiles of Pd/xSn(10-x)Zr catalysts, dependence of catalytic activity (TOF at 280 °C) on the oxygen desorption temperature (B) (obtained by O₂-TPD), PdO_x content (D) (determined by O₂-TPO), and PdO reduction temperature (F) (obtained by CH₄-TPR) of catalysts.

and the easily released lattice oxygen species [24]. From Fig. 5B, the temperature of the oxygen desorption peak of PdO on catalysts was well-related to the catalytic activity. Methane combustion over Pd-based catalysts generally follows the Mars-van-Krevelen mechanism, where the lattice oxygen of PdO reacts with methane [6,14,56]. For Pd/7.2Sn2.8Zr, the lattice oxygen of PdO was liable to desorb, indicating a high reactivity, which led to a superior catalytic activity.

The redox of Pd \leftrightarrow PdO over catalysts was further explored through O₂-TPO experiments. Compared with the TPO profiles of supports (Fig. S9B), the oxygen release peaks of catalysts (Fig. 5C) at 750–900 °C during the heating process were assigned to the decomposition of PdO species, while the oxygen consumption peaks at 550–720 °C during the cooling stage belonged to the reoxidation of Pd to PdO [57]. As shown in the deconvolution results (Fig. S10), the broad PdO decomposition peaks over catalysts suggested the presence of different PdO species: PdO in contact with metal Pd (α), bulk PdO (β), and PdO that interacted strongly with supports (γ) [58–60]. The α species could be associated with the partially oxidized palladium species (PdO_x), which consisted of PdO and Pd patches with a distinct oxide interphase between them [61]. The ratio of α species on Pd/7.2Sn2.8Zr was relatively high (Table S8), demonstrating the presence of a higher content of PdO_x, which was consistent with the observation of several amorphous PdO_x particles on Pd/7.2Sn2.8Zr (Fig. 4C). Fig. 5D illustrated that the increase of PdO_x content had a significant correlation with the improvement of catalytic activity, indicating that the PdO_x species was beneficial to the oxidation of methane, which was in line with the previous finding [51]. Besides, the hysteresis between PdO decomposition and Pd reoxidation was quite small over Pd/7.2Sn2.8Zr, demonstrating a facile conversion of Pd \leftrightarrow PdO. This could be ascribed to the generation of oxygen vacancies and the enhancement of oxygen mobility, which facilitated the regeneration of PdO, provoking excellent catalytic activity and stability even under wet conditions.

The reducibility of catalysts was studied via CH₄-TPR experiments.

As illustrated in Fig. 5E and Fig. S11, the consumption of methane and the release of CO₂ and H₂O were detected at 290–345 °C (Phase I), indicating the reaction between CH₄ and PdO species (CH₄ + 4 PdO → 4 Pd + CO₂ + 2 H₂O) [62]. The above consumption peak of Pd/7.2Sn2.8Zr was at a lower temperature than that of other catalysts, verifying the high reducibility of PdO and the weak Pd-O bond, which matched well with O₂-TPD analysis. Moreover, H₂-TPR experiments (Fig. S12A) also confirmed the higher reducibility of PdO over Pd/7.2Sn2.8Zr. The reduction temperature of PdO was well correlated with the catalytic activity (Fig. 5F), implying that the reducibility of PdO had a critical impact on methane combustion. The high-temperature H₂-TPR profiles of catalysts (Fig. S12B) revealed that the incorporation of an appropriate content of Zr improved the reducibility of SnO₂ in catalysts, which could be ascribed to the weakened Sn-O bond due to the formation of Sn_xZr_{1-x}O₂ solid solutions. With the increase of Zr content, the consumption peaks of CH₄-TPR profiles at above 350 °C (Phase II and III) became more intense over Zr-rich catalysts, accompanied by a significant release of H₂ and a weak release of CO (Fig. S11). It is inferred that the Zr component would promote the steam reforming reaction (CH₄ + H₂O → CO + 3 H₂) and the methane cracking reaction (CH₄ → C + 2 H₂) [60]. The inferior catalytic stability of Pd/10Zr may result from the formation of coke due to the cracking reaction. In addition, the low content of active PdO_x and the inferior reducibility of PdO on Pd/ZrO₂ may be responsible for the low catalytic activity and the slow conversion of methane at high temperatures (>400 °C) during light-off tests (Fig. 1A). Based on above analysis, it could be deduced that the formation of a higher content of Sn_xZr_{1-x}O₂ solid solution in Pd/7.2Sn2.8Zr generated abundant oxygen vacancies, which enhanced the oxygen mobility of catalysts, improved the reducibility of PdO and the conversion of Pd \leftrightarrow PdO. Moreover, the formation of Sn_xZr_{1-x}O₂ solid solution would give rise to highly active PdO_x species, conjointly leading to the superior catalytic activity, stability and water-resistance towards methane combustion.

3.3. Analysis on the sulfur poisoning and regeneration of catalysts

As shown in the TEM images of catalysts (Fig. S6), the particle sizes of sulfated Pd/10Sn and Pd/7.2Sn2.8Zr were similar with those of corresponding fresh catalysts. The particle size of sulfated Pd/10Zr increased significantly, manifesting severe sintering of the catalyst, which may cause the obvious deactivation under sulfur-containing conditions. From HRTEM images of sulfated catalysts (Fig. S13), the interplanar spacings ascribed to PdO, SnO₂ and ZrO₂ phase were observed. Different from the fresh Pd/7.2Sn2.8Zr catalyst, amorphous PdO_x particles were hardly detected after sulfidation. Moreover, the aggregation of palladium species in sulfated Pd/10Zr and Pd/7.2Sn2.8Zr could be clearly observed from HAADF-STEM images (Fig. 6) compared with corresponding fresh catalysts (Fig. S7). The sintering of active palladium species in sulfur-containing atmosphere would result in the diminish of active sites [63], which may constitute one of the reasons for the loss of activity. In comparison, the palladium species of sulfated Pd/10Sn remained a relatively high dispersion and small particle size, which was favorable to methane combustion in a sulfur-containing atmosphere. The EDS mapping images revealed the uniform distribution of sulfur species over catalysts, suggesting that sulfur species were mainly accumulated on the support [63], which existed as sulfates or sulfites as revealed by the FTIR spectra of fresh and sulfated catalysts (Fig. S14).

The influence of sulfur-containing atmosphere on the surface sites of palladium species was further explored. From the CO-DRIFTS of fresh catalysts (Fig. S15), bands attributed to the linear adsorption of CO on Pd corner sites or Pd (111) plane (ca. 2085 cm⁻¹), bridge-bonded CO at the step sites (ca. 1974 cm⁻¹), and bridge-bonded CO at hollow sites of Pd (111) (1850–1951 cm⁻¹) were identified [64–66]. According to the Gaussian fitting results (Table S9), Pd/7.2Sn2.8Zr had a higher proportion of Pd step sites, which may be associated with the presence of more active PdO_x species. The surface sites of the palladium species on the sulfated and regenerated catalysts were different from those on the corresponding fresh catalysts. For the sulfated Pd/10Sn (Fig. 7A), the band at ca. 1974 cm⁻¹ became more intense, suggesting the increase of Pd step sites (Table S9). Meanwhile, the band of bridge-bonded CO at

hollow sites of Pd (111) shifted to a higher wavenumber (from 1850 to 1920 cm⁻¹), indicating a weakened electron back-donation from the hollow site of Pd to the bridge-bonded CO. However, the bands ascribed to Pd step sites on sulfated Pd/10Zr and Pd/7.2Sn2.8Zr (Fig. 7B and C) were weakened compared with fresh ones, which may be due to the sintering of Pd particles, or the coverage of sulfur species on catalysts [67], resulting in the decrease of active sites and loss of catalytic activity. After regeneration, the band ascribed to Pd step sites still could be observed on Pd/10Sn (Fig. 7D), while it was absent on Pd/10Zr and Pd/7.2Sn2.8Zr (Fig. 7E and F). Considering the superior catalytic performance of Pd/10Sn under SO₂-containing conditions and after regeneration, it is deduced that the step sites of Pd particles were active for methane combustion, which would be poisoned by sulfur species and induce the deactivation of catalysts.

The oxygen mobility and oxygen vacancies of catalysts were also affected by the sulfur species. From O₂-TPD profiles of fresh/sulfated supports and catalysts (Fig. 8A and B), the oxygen species on sulfated supports desorbed at higher temperatures than corresponding fresh supports, indicating that the accumulation of sulfur species inhibited the oxygen mobility. For sulfated Pd/7.2Sn2.8Zr, the lattice oxygen of PdO desorbed at a higher temperature than the fresh one, which may result from the sintering of palladium species, exerting negative influences on methane oxidation. The lattice oxygen of PdO in sulfated Pd/10Sn desorbed at a slightly higher temperature compared to the fresh one. Coupled with the maintained particle size of PdO, Pd/10Sn could afford a relatively high catalytic activity in sulfur-containing atmosphere. Although the oxygen desorption temperature of sulfated Pd/10Zr was similar to that of the fresh one, its desorption peak was relatively weak, indicating a lower content of PdO species on Pd/10Zr, which led to the inferior catalytic performance.

The electrical conductivity of fresh/sulfated/regenerated catalysts was investigated to explore the variation in oxygen vacancies of catalysts, as the concentration of oxygen vacancies could be reflected by the oxide ionic conducting properties [68,69]. From Fig. 8C, the conductivity of fresh Pd/7.2Sn2.8Zr was 1–3 orders of magnitude higher than those of fresh Pd/10Sn and Pd/10Zr at the same temperature, indicating the presence of abundant oxygen vacancies in Pd/7.2Sn2.8Zr, which

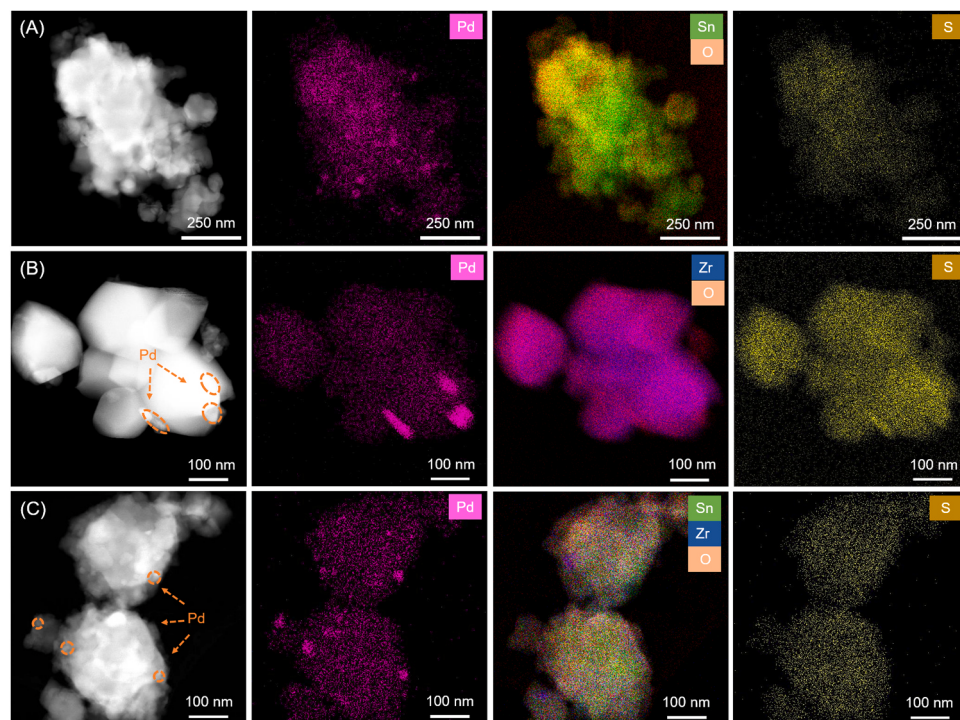


Fig. 6. HAADF-STEM images and EDS elemental mapping (Pd, Sn, Zr, O, S) of sulfated Pd/10Sn (A), Pd/10Zr (B) and Pd/7.2Sn2.8Zr (C) catalysts.

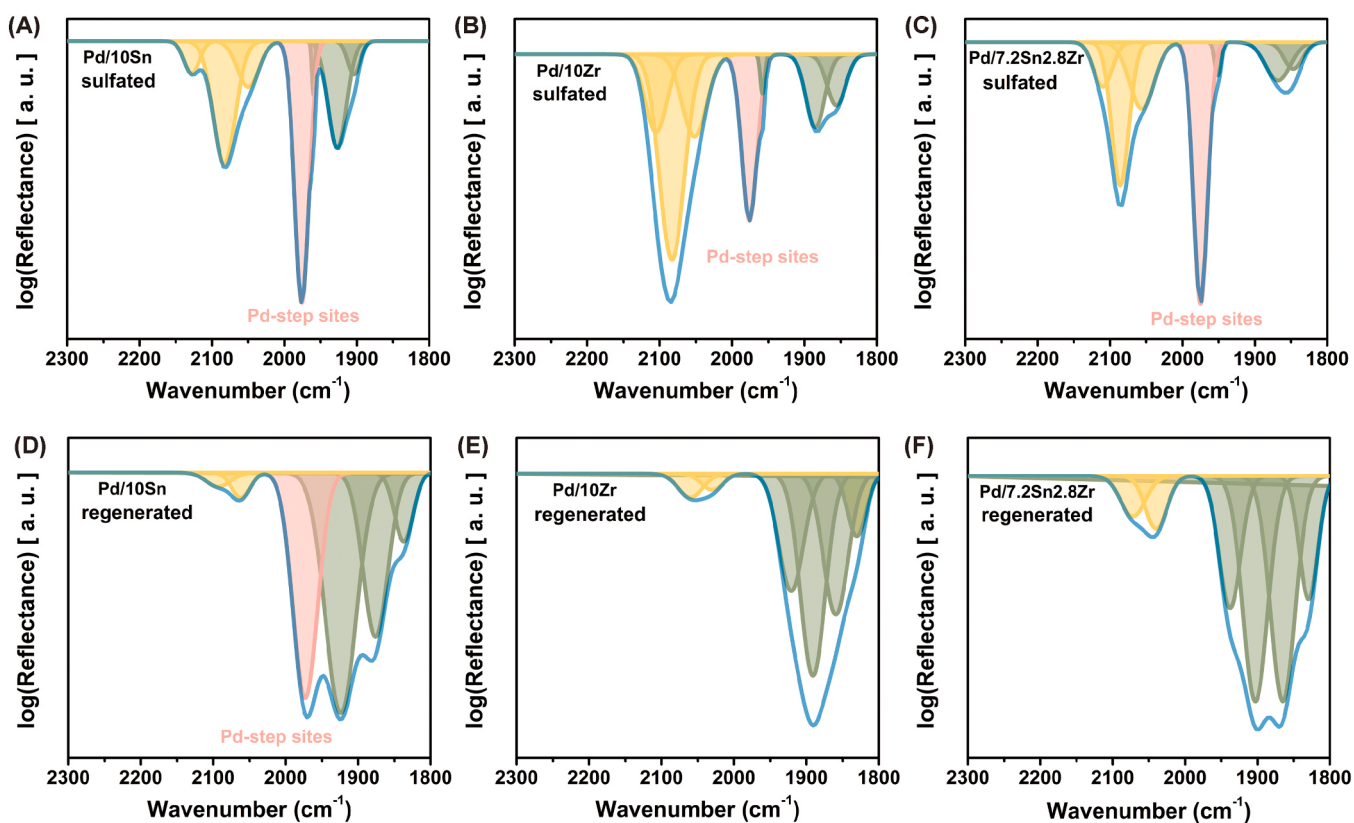
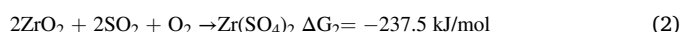


Fig. 7. CO-DRIFTS of sulfated and regenerated Pd/10Sn (A, D), Pd/10Zr (B, E) and Pd/7.2Sn2.8Zr (C, F) catalysts.

may be related to the formation of more $\text{Sn}_x\text{Zr}_{1-x}\text{O}_2$ solid solutions. The conductivity of sulfated Pd/10Sn was slightly lower than that of the fresh one, while the conductivity of sulfated Pd/10Zr and Pd/7.2Sn2.8Zr decreased significantly. Considering that the content of sulfur species (Table S10) detected on sulfated Pd/10Zr and Pd/7.2Sn2.8Zr was higher than that on Pd/10Sn, it is inferred that the lowered electrical conductivity may be due to the accumulation of sulfur species on the support, which caused the diminish of oxygen vacancies. After regeneration, the conductivity of Pd/10Sn was even higher than that of the fresh one. Although the conductivities of the regenerated Pd/10Zr and Pd/7.2Sn2.8Zr catalysts also increased to some extent, they were still lower than those of corresponding fresh catalysts. Given the correlation between the conductivity and activity of the catalysts under different treatments (Fig. 8D), it is inferred that the formation of oxygen vacancies was crucial for methane oxidation.

As for the SnO_2 and ZrO_2 supports, the formation of sulfates in oxygen-containing atmosphere is a spontaneous process according to the Gibbs energies ($<0 \text{ kJ/mol}$) of the following reactions, and the formation of $\text{Zr}(\text{SO}_4)_2$ is more thermodynamically favorable.



Besides, the bond energy of $D_{\text{S-Sn}}^\Theta$ (467 kJ/mol) is lower than that of $D_{\text{S-Zr}}^\Theta$ (572 kJ/mol), implying that $\text{Zr}(\text{SO}_4)_2$ is more stable than $\text{Sn}(\text{SO}_4)_2$. Therefore, sulfur species were more liable to accumulate on the Zr-containing catalysts and were more difficult to decompose, which would block the oxygen vacancies. The diminish of oxygen vacancies was adverse to the regeneration of PdO , leading to the sintering of palladium particles and the loss of active Pd step sites, which resulted in the deactivation of catalysts. Hence, preserving the content of oxygen vacancies and active palladium species on catalysts is the key to maintaining an efficient reaction, which is highly dependent on the metal-support interaction.

4. Conclusions

Binary oxides composed of SnO_2 and ZrO_2 in different molar ratios were prepared by co-precipitation and hydrothermal crystallization route, and Pd-based catalysts for methane combustion were constructed using them as supports. $\text{Sn}_x\text{Zr}_{1-x}\text{O}_2$ solid solutions formed in catalysts with lower $n_{\text{Zr}}/n_{\text{Sn}}$ ratios (<1), while $\text{Sn}_x\text{Zr}_{1-x}\text{O}_2$ solid solutions and ZrO_2 coexisted in catalysts with higher $n_{\text{Zr}}/n_{\text{Sn}}$ ratios (≥ 1). The promoted formation of $\text{Sn}_x\text{Zr}_{1-x}\text{O}_2$ solid solutions in Pd/7.2Sn2.8Zr induced the generation of oxygen vacancies and active PdO_x species, giving rise to a superior catalytic activity and hydrothermal stability compared to Pd/ ZrO_2 and Pd/ SnO_2 catalysts. Under sulfur-containing reaction conditions, the more readily formation of stable $\text{Zr}(\text{SO}_4)_2$ on Zr-containing catalysts caused the decrease of oxygen vacancies and active Pd step sites, resulting in the deactivation of catalysts and the insufficient regeneration performance. By contrast, the Pd/ SnO_2 catalysts exhibited an improved sulfur-resistance due to the better retained oxygen vacancies and active Pd step sites, manifesting that oxygen vacancies and active palladium species were crucial for methane combustion. The revealed support effect and structure-performance relationship can be extended to construct high-performance Pd-based catalysts for catalytic oxidation reactions.

CRediT authorship contribution statement

Jia Lin: Investigation, formal analysis, data curation, writing – original draft. **Jiangli Huang:** Investigation, formal analysis, data curation. **Xiaohua Chen:** Methodology, validation. **Yong Zheng:** Visualization, Investigation. **Yihong Xiao:** Resources, Methodology. **Ying Zheng:** Conceptualization, Methodology, Formal analysis, Supervision, Project administration, Writing - review & editing. **Lilong Jiang:** Resources, Supervision, Project administration.

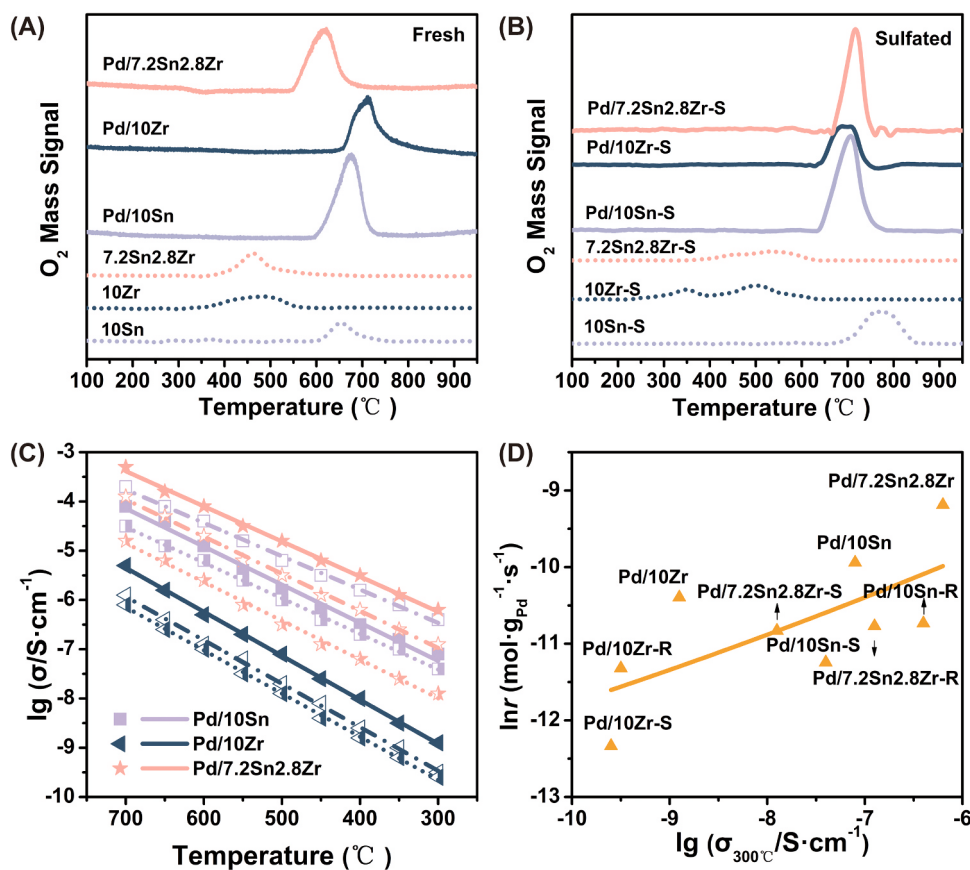


Fig. 8. O₂-TPD profiles of fresh (A) and sulfated (B) supports and catalysts, temperature dependence of the conductivity values for fresh (solid symbol), sulfated (half-right symbol) and regenerated (open symbol) catalysts (C), dependence of catalytic activity (reaction rate at 280 °C) on the conductivity of fresh, sulphated (-S) and regenerated (-R) catalysts (D).

Declaration of Competing Interest

The authors declare that they have no known competing financial interests or personal relationships that could have appeared to influence the work reported in this paper.

Data availability

The authors are unable or have chosen not to specify which data has been used.

Acknowledgment

This work was supported by the National Natural Science Foundation of China (Nos. 22272023 and 22108036).

Appendix A. Supporting information

Supplementary data associated with this article can be found in the online version at doi:10.1016/j.apcatb.2023.123283.

References

- [1] L. He, Y. Fan, J. Bellettre, J. Yue, L. Luo, A review on catalytic methane combustion at low temperatures: catalysts, mechanisms, reaction conditions and reactor designs, *Renew. Sustain. Energy Rev.* 119 (2020), 109589.
- [2] J. Wang, R. Fu, S. Wen, P. Ning, M.H. Helal, M.A. Salem, B.B. Xu, Z.M. El-Bahy, M. Huang, Z. Guo, L. Huang, Q. Wang, Progress and current challenges for CO₂ capture materials from ambient air, *Adv. Compos. Hybrid Mater.* 5 (2022) 2721–2759.
- [3] S.L. Hamukwaya, Z. Zhao, H. Hao, H.M. Abo-Dief, K.M. Abualnaja, A.K. Alanazi, M. Mashingaidze, S.M. El-Bahy, M. Huang, Z. Guo, Enhanced photocatalytic performance for hydrogen production and carbon dioxide reduction by a mesoporous single-crystal-like TiO₂ composite catalyst, *Adv. Compos. Hybrid Mater.* 5 (2022) 2620–2630.
- [4] D. Ping, F. Yi, G. Zhang, S. Wu, S. Fang, K. Hu, B.B. Xu, J. Ren, Z. Guo, NH₄Cl-assisted preparation of single Ni sites anchored carbon nanosheet catalysts for highly efficient carbon dioxide electroreduction, *J. Mater. Sci. Technol.* 142 (2023) 1–9.
- [5] Y. Cao, M. Weng, M.H.H. Mahmoud, A.Y. Elnaggar, L. Zhang, I.H. El Azab, Y. Chen, M. Huang, J. Huang, X. Sheng, Flame-retardant and leakage-proof phase change composites based on MXene/polyimide aerogels toward solar thermal energy harvesting, *Adv. Compos. Hybrid Mater.* 5 (2022) 1253–1267.
- [6] Z. Tang, T. Zhang, D. Luo, Y. Wang, Z. Hu, R.T. Yang, Catalytic combustion of methane: From mechanism and materials properties to catalytic performance, *ACS Catal.* 12 (2022) 13457–13474.
- [7] Q. Hu, J. Zhou, B. Qiu, Q. Wang, G. Song, Z. Guo, Synergistically improved methane production from anaerobic wastewater treatment by iron/polyaniline composite, *Adv. Compos. Hybrid Mater.* 4 (2021) 265–273.
- [8] X. Yang, Q. Gao, Z. Zhao, Y. Guo, Y. Guo, L. Wang, Y. Wang, W. Zhan, Surface tuning of noble metal doped perovskite oxide by synergistic effect of thermal treatment and acid etching: A new path to high-performance catalysts for methane combustion, *Appl. Catal. B: Environ.* 239 (2018) 373–382.
- [9] X. Meng, H. Yang, Z. Lu, Y. Liu, Study on catalytic pyrolysis and combustion characteristics of waste cable sheath with crosslinked polyethylene, *Adv. Compos. Hybrid Mater.* 5 (2022) 2948–2963.
- [10] W. Huang, A.C. Johnston-Peck, T. Wolter, W.-C.D. Yang, L. Xu, J. Oh, B.A. Reeves, C. Zhou, M.E. Holtz, A.A. Herzing, A.M. Lindenberg, M. Mavrikakis, M. Cargnello, Steam-created grain boundaries for methane C-H activation in palladium catalysts, *Science* 373 (2021) 1518–1523.
- [11] L. Wang, S. Lyu, P. Zhang, X. Tian, D. Wang, W. Huang, Z. Liu, Nitrogen-bonded ultrasmall palladium clusters over the nitrogen-doped carbon for promoting Suzuki cross-coupling reactions, *Adv. Compos. Hybrid Mater.* 5 (2022) 1396–1403.
- [12] Z. Liu, G. Xu, L. Zeng, W. Shi, Y. Wang, Y. Sun, Y. Yu, H. He, Anchoring Pt-doped PdO nanoparticles on γ-Al₂O₃ with highly dispersed La sites to create a methane oxidation catalyst, *Appl. Catal. B: Environ.* 324 (2023), 122259.
- [13] K. Murata, D. Kosuge, J. Ohyama, Y. Mahara, Y. Yamamoto, S. Arai, A. Satsuma, Exploiting metal-support interactions to tune the redox properties of supported Pd catalysts for methane combustion, *ACS Catal.* 10 (2020) 1381–1387.

[14] X. Zou, J. Chen, Z. Rui, H. Ji, Sequential growth reveals multi-spinel interface promotion for methane combustion over alumina supported palladium catalyst, *Appl. Catal. B: Environ.* 273 (2020), 119071.

[15] Z. Zhang, L. Sun, X. Hu, Y. Zhang, H. Tian, X. Yang, Anti-sintering Pd@silicalite-1 for methane combustion: Effects of the moisture and SO₂, *Appl. Surf. Sci.* 494 (2019) 1044–1054.

[16] J. Lin, L. Zhao, Y. Zheng, Y. Xiao, G. Yu, Y. Zheng, W. Chen, L. Jiang, Facile strategy to extend stability of simple component-alumina-supported palladium catalysts for efficient methane combustion, *ACS Appl. Mater. Interfaces* 12 (2020) 56095–56107.

[17] H. Xiong, D. Kunwar, D. Jiang, C.E. García-Vargas, H. Li, C. Du, G. Canning, X. I. Pereira-Hernandez, Q. Wan, S. Lin, S.C. Purdy, J.T. Miller, K. Leung, S.S. Chou, H.H. Brongersma, R. ter Veen, J. Huang, H. Guo, Y. Wang, A.K. Datye, Engineering catalyst supports to stabilize PdO_x two-dimensional rafts for water-tolerant methane oxidation, *Nat. Catal.* 4 (2021) 830–839.

[18] C. Hou, W. Yang, H. Kimura, X. Xie, X. Zhang, X. Sun, Z. Yu, X. Yang, Y. Zhang, B. Wang, B.B. Xu, D. Sridhar, H. Aljadi, Z. Guo, W. Du, Boosted lithium storage performance by local build-in electric field derived by oxygen vacancies in 3D holey N-doped carbon structure decorated with molybdenum dioxide, *J. Mater. Sci. Technol.* 142 (2023) 185–195.

[19] K. Xie, S. Wei, A. Alhadhrami, J. Liu, P. Zhang, A.Y. Elnaggar, F. Zhang, M.H. H. Mahmoud, V. Murugadoss, S.M. El-Bahy, F. Wang, C. Li, G. Li, Synthesis of CsPbBr₃/CsPb₂Br₃@silica yolk-shell composite microspheres: precisely controllable structure and improved catalytic activity for dye degradation, *Adv. Compos. Hybrid Mater.* 5 (2022) 1423–1432.

[20] Z. Wang, C. Tang, J. Lin, Y. Zheng, Y. Xiao, Y. Zheng, L. Jiang, Promoting methane combustion activity and stability by tuning multiple Ni-Si interactions in catalysts, *Fuel* 349 (2023), 128678.

[21] J. Xu, L. Ouyang, W. Mao, X.-J. Yang, X.-C. Xu, J.-J. Su, T.-Z. Zhuang, H. Li, Y.-F. Han, Operando and kinetic study of low-temperature, lean-burn methane combustion over a Pd/γ-Al₂O₃ catalyst, *ACS Catal.* 2 (2012) 261–269.

[22] J. Shen, R.E. Hayes, N. Semagina, On the contribution of oxygen from Co₃O₄ to the Pd-catalyzed methane combustion, *Catal. Today* 360 (2021) 435–443.

[23] T. Wang, L. Qiu, H. Li, C. Zhang, Y. Sun, S. Xi, J. Ge, Z.J. Xu, C. Wang, Facile synthesis of palladium incorporated NiCo₂O₄ spinel for low temperature methane combustion: Activate lattice oxygen to promote activity, *J. Catal.* 404 (2021) 400–410.

[24] Y. Wu, J. Chen, W. Hu, K. Zhao, P. Qu, P. Shen, M. Zhao, L. Zhong, Y. Chen, Phase transformation and oxygen vacancies in Pd/ZrO₂ for complete methane oxidation under lean conditions, *J. Catal.* 377 (2019) 565–576.

[25] H. Peng, C. Rao, N. Zhang, X. Wang, W. Liu, W. Mao, L. Han, P. Zhang, S. Dai, Confined ultrathin Pd-Ce nanowires with outstanding moisture and SO₂ tolerance in methane combustion, *Angew. Chem. Int. Ed.* 57 (2018) 8953–8957.

[26] Y. Wang, C. Liu, X. Liao, Y. Liu, J. Hou, C. Pham-Huu, Enhancing oxygen activation on high surface area Pd-SnO₂ solid solution with isolated metal site catalysts for catalytic CH₄ combustion, *Appl. Surf. Sci.* 564 (2021), 150368.

[27] W. Barrett, J. Shen, Y. Hu, R.E. Hayes, R.W.J. Scott, N. Semagina, Understanding the role of SnO₂ support in water-tolerant methane combustion: in situ observation of Pd(OH)₂ and comparison with Pd/Al₂O₃, *ChemCatChem* 12 (2020) 944–952.

[28] M. Danielis, S. Colussi, C. de leitenburg, L. Soler, J. Llorca, A. Trovarelli, Outstanding methane oxidation performance of Pd-embedded ceria catalysts prepared by a one-step dry ball-milling method, *Angew. Chem. Int. Ed.* 57 (2018) 10212–10216.

[29] N. Zhang, Y. Guo, Y. Guo, Q. Dai, L. Wang, S. Dai, W. Zhan, Synchronously constructing the optimal redox-acidity of sulfate and RuO_x Co-modified CeO₂ for catalytic combustion of chlorinated VOCs, *Chem. Eng. J.* 454 (2023), 140391.

[30] W. Yang, F. Polo-Garzon, H. Zhou, Z. Huang, M. Chi, H. Meyer, X. Yu, Y. Li, Z. Wu, Boosting the activity of Pd single atoms by tuning their local environment on ceria for methane combustion, *Angew. Chem. Int. Ed.* 62 (2023), e202217323.

[31] J. Huang, J. Lin, X. Chen, Y. Zheng, Y. Xiao, Y. Zheng, Optimizing the microstructure of SnO₂-CeO₂ binary oxide supported palladium catalysts for efficient and stable methane combustion, *ACS Appl. Mater. Interfaces* 14 (2022) 16233–16244.

[32] E. Hong, C. Kim, D.-H. Lim, H.-J. Cho, C.-H. Shin, Catalytic methane combustion over Pd/ZrO₂ catalysts: Effects of crystalline structure and textural properties, *Appl. Catal. B: Environ.* 232 (2018) 544–552.

[33] Y. Ding, Q. Wu, B. Lin, Y. Guo, Y. Guo, Y. Wang, L. Wang, W. Zhan, Superior catalytic activity of a Pd catalyst in methane combustion by fine-tuning the phase of ceria-zirconia support, *Appl. Catal. B: Environ.* 266 (2020), 118631.

[34] Y. Ding, Y. Jia, M. Jiang, Y. Guo, Y. Guo, L. Wang, Q. Ke, M.N. Ha, S. Dai, W. Zhan, Superior catalytic activity of Pd-based catalysts upon tuning the structure of the ceria-zirconia support for methane combustion, *Chem. Eng. J.* 416 (2021), 129150.

[35] W. Yang, M.-Y. Kim, F. Polo-Garzon, J. Gong, X. Jiang, Z. Huang, M. Chi, X. Yu, X. Wang, Y. Guo, Z. Wu, CH₄ combustion over a commercial Pd/CeO₂-ZrO₂ three-way catalyst: Impact of thermal aging and sulfur exposure, *Chem. Eng. J.* 451 (2023), 138930.

[36] W. Lin, L. Lin, Y.X. Zhu, Y.C. Xie, K. Scheurell, E. Kemnitz, Novel Pd/Sn_xZr_{1-x}O₂ catalysts for methane total oxidation at low temperature and their ¹⁸O-isotope exchange behavior, *Appl. Catal. B: Environ.* 57 (2005) 175–181.

[37] M. Monai, T. Montini, M. Melchionna, T. Duchoñ, P. Kúš, C. Chen, N. Tsud, L. Nasi, K.C. Prince, K. Veltruská, V. Matolín, M.M. Khader, R.J. Gorte, P. Fornasiero, The effect of sulfur dioxide on the activity of hierarchical Pd-based catalysts in methane combustion, *Appl. Catal. B: Environ.* 202 (2017) 72–83.

[38] F. Polo-Garzon, Z. Bao, X. Zhang, W. Huang, Z. Wu, Surface reconstructions of metal oxides and the consequences on catalytic chemistry, *ACS Catal.* 9 (2019) 5692–5707.

[39] X. Li, X. Wang, K. Roy, J.A. van Bokhoven, L. Artiglia, Role of water on the structure of palladium for complete oxidation of methane, *ACS Catal.* 10 (2020) 5783–5792.

[40] J.-H. Park, J.H. Cho, Y.J. Kim, E.S. Kim, H.S. Han, C.-H. Shin, Hydrothermal stability of Pd/ZrO₂ catalysts for high temperature methane combustion, *Appl. Catal. B: Environ.* 160–161 (2014) 135–143.

[41] Z. Pu, Y. Liu, H. Zhou, W. Huang, Y. Zheng, X. Li, Catalytic combustion of lean methane at low temperature over ZrO₂-modified Co₃O₄ catalysts, *Appl. Surf. Sci.* 422 (2017) 85–93.

[42] J. Xiong, K. Wu, J. Yang, P. Liu, L. Song, J. Zhang, M. Fu, L. Chen, H. Huang, J. Wu, D. Ye, The effect of existence states of PdO_x supported by Co₃O₄ nanoplatelets on catalytic oxidation of methane, *Appl. Surf. Sci.* 539 (2021), 148211.

[43] S. Xie, E. Iglesia, A.T. Bell, Water-assisted tetragonal-to-monoclinic phase transformation of ZrO₂ at low temperatures, *Chem. Mater.* 12 (2000) 2442–2447.

[44] X. Yao, Y. Xiong, W. Zou, L. Zhang, S. Wu, X. Dong, F. Gao, Y. Deng, C. Tang, Z. Chen, L. Dong, Y. Chen, Correlation between the physicochemical properties and catalytic performances of Ce_xSn_{1-x}O₂ mixed oxides for NO reduction by CO, *Appl. Catal. B: Environ.* 144 (2014) 152–165.

[45] C. Liu, H. Xian, Z. Jiang, L. Wang, J. Zhang, L. Zheng, Y. Tan, X. Li, Insight into the improvement effect of the Ce doping into the SnO₂ catalyst for the catalytic combustion of methane, *Appl. Catal. B: Environ.* 176–177 (2015) 542–552.

[46] J. Lin, Y. Xu, X. Chen, J. Huang, H. Xu, Y. Zheng, Electron promoted palladium-cobalt active sites for efficient catalytic combustion of methane, *J. Clean. Prod.* 385 (2023), 135744.

[47] S.N. Basahel, T.T. Ali, M. Mokhtar, K. Narasimharao, Influence of crystal structure of nanosized ZrO₂ on photocatalytic degradation of methyl orange, *Nanoscale Res. Lett.* 10 (2015), 73.

[48] X. Yang, L. Yang, S. Lin, R. Zhou, New insight into the doping effect of Pr₂O₃ on the structure-activity relationship of Pd/CeO₂-ZrO₂ catalysts by Raman and XRD rietveld analysis, *J. Phys. Chem. C* 119 (2015) 6065–6074.

[49] E.M. Slavinskaya, A.V. Zadesenets, O.A. Stonkus, A.I. Stadnichenko, A. V. Shchukarev, Y.V. Shubin, S.V. Korenev, A.I. Boronin, Thermal activation of Pd/CeO₂-SnO₂ catalysts for low-temperature CO oxidation, *Appl. Catal. B: Environ.* 277 (2020), 119275.

[50] E.M. Slavinskaya, R.V. Gulyaev, A.V. Zadesenets, O.A. Stonkus, V.I. Zaikovskii, Y. V. Shubin, S.V. Korenev, A.I. Boronin, Low-temperature CO oxidation by Pd/CeO₂ catalysts synthesized using the coprecipitation method, *Appl. Catal. B: Environ.* 166–167 (2015) 91–103.

[51] E.J. Jang, J. Lee, D.G. Oh, J.H. Kwak, CH₄ oxidation activity in Pd and Pt-Pd bimetallic catalysts: Correlation with surface PdO_x quantified from the DRIFTS study, *ACS Catal.* 11 (2021) 5894–5905.

[52] M.D. Farahani, M. Wolf, T. P.O. Mkhwanazi, M. Claeys, H.B. Friedrich, Operando experimental evidence on the central role of oxygen vacancies during methane combustion, *J. Catal.* 390 (2020) 184–195.

[53] Y. Zheng, K. Li, H. Wang, Y. Wang, D. Tian, Y. Wei, X. Zhu, C. Zeng, Y. Luo, Structure dependence and reaction mechanism of CO oxidation: A model study on macroporous CeO₂ and CeO₂-ZrO₂ catalysts, *J. Catal.* 344 (2016) 365–377.

[54] Q. Wang, L. Chen, S. Guan, X. Zhang, B. Wang, X. Cao, Z. Yu, Y. He, D.G. Evans, J. Feng, D. Li, Ultrathin and vacancy-rich CoAl-layered double hydroxide/graphite oxide catalysts: Promotional effect of cobalt vacancies and oxygen vacancies in alcohol oxidation, *ACS Catal.* 8 (2018) 3104–3115.

[55] X. Zou, Z. Rui, S. Song, H. Ji, Enhanced methane combustion performance over NiAl₂O₄-interface-promoted Pd/γ-Al₂O₃, *J. Catal.* 338 (2016) 192–201.

[56] G. Zhao, X. Pan, Z. Zhang, Y. Liu, Y. Lu, A thin-felt Pd-MgO-Al₂O₃/Al-fiber catalyst for catalytic combustion of methane with resistance to water-vapor poisoning, *J. Catal.* 384 (2020) 122–135.

[57] W. Li, D. Liu, X. Feng, Z. Zhang, X. Jin, Y. Zhang, High-performance ultrathin Co₃O₄ nanosheet supported PdO/CeO₂ catalysts for methane combustion, *Adv. Energy Mater.* 9 (2019), 1803583.

[58] H. Duan, R. You, S. Xu, Z. Li, K. Qian, T. Cao, W. Huang, X. Bao, Penta-coordinated Al³⁺-stabilized active Pd structures on Al₂O₃ coated palladium catalysts for methane combustion, *Angew. Chem. Int. Ed.* 58 (2019) 12043–12048.

[59] A. Toso, S. Colussi, S. Padigapati, C. de Leitenburg, A. Trovarelli, High stability and activity of solution combustion synthesized Pd-based catalysts for methane combustion in presence of water, *Appl. Catal. B: Environ.* 230 (2018) 237–245.

[60] N. Sadokhina, G. Smedler, U. Nylen, M. Olofsson, L. Olsson, The influence of gas composition on Pd-based catalyst activity in methane oxidation-inhibition and promotion by NO, *Appl. Catal. B: Environ.* 200 (2017) 351–360.

[61] R.J. Bunting, X. Cheng, J. Thompson, P. Hu, Amorphous surface PdO_x and its activity towards methane combustion, *ACS Catal.* 9 (2019) 10317–10323.

[62] I. Friberg, N. Sadokhina, L. Olsson, The effect of Si/Al ratio of zeolite supported Pd for complete CH₄ oxidation in the presence of water vapor and SO₂, *Appl. Catal. B: Environ.* 250 (2019) 117–131.

[63] J. Lin, X. Chen, Y. Zheng, Y. Xiao, Y. Zheng, L. Jiang, Sulfur-resistant methane combustion invoked by surface property regulation on palladium-based catalysts, *Appl. Surf. Sci.* 587 (2022), 152835.

[64] J. Chen, J. Zhong, Y. Wu, W. Hu, P. Qu, X. Xiao, G. Zhang, X. Liu, Y. Jiao, L. Zhong, Y. Chen, Particle size effects in stoichiometric methane combustion: Structure-activity relationship of Pd catalyst supported on gamma-alumina, *ACS Catal.* 10 (2020) 10339–10349.

[65] K. Murata, Y. Mahara, J. Ohyama, Y. Yamamoto, S. Arai, A. Satsuma, The metal-support interaction concerning the particle size effect of Pd/Al₂O₃ on methane combustion, *Angew. Chem. Int. Ed.* 56 (2017) 15993–15997.

[66] M. Peter, J.M. Flores Camacho, S. Adamowski, L.K. Ono, K.H. Dostert, C.P. O'Brien, B.R. Cuenya, S. Schauermann, H.J. Freund, Trends in the binding strength of

surface species on nanoparticles: how does the adsorption energy scale with the particle size? *Angew. Chem. Int. Ed.* 52 (2013) 5175–5179.

[67] Y. Ding, S. Wang, L. Zhang, L. Lv, D. Xu, W. Liu, S. Wang, Investigation of supported palladium catalysts for combustion of methane: The activation effect caused by SO₂, *Chem. Eng. J.* 382 (2020), 122969.

[68] L.M. Madeira, J.M. Herrmann, F.G. Freire, M.F. Portela, F.J. Maldonado, Electrical conductivity, basicity and catalytic activity of Cs-promoted α -NiMoO₄ catalysts for the oxidative dehydrogenation of n-butane, *Appl. Catal. A: Gen.* 158 (1997) 243–256.

[69] T. Kaur, K. Singh, J. Kolte, Effect of intrinsic and extrinsic oxygen vacancies on the conductivity of Gd-doped CeO₂ synthesized by a sonochemical route, *J. Phys. Chem. C* 126 (2022) 18018–18028.